ACS APPLIED MATERIALS & INTERFACES

Letter

www.acsami.org

Efficient and Balanced Charge Transport Revealed in Planar Perovskite Solar Cells

Yani Chen,† Jiajun Peng,† Diqing Su, Xiaoqing Chen, and Ziqi Liang*

Department of Materials Science, Fudan University, Shanghai 200433, China

Supporting Information

ABSTRACT: Hybrid organic−inorganic perovskites have emerged as novel photovoltaic materials and hold great promise for realization of high-efficiency thin film solar modules. In this study, we unveil the ambipolar characteristics of perovskites by employing the transport measurement techniques of charge extraction by linearly increasing voltage (CELIV) and time-of-flight (TOF). These two complementary methods are combined to quantitatively determine the mobilities of hole and electron of $CH_3NH_3PbI_3$ perovskite while revealing the recombination process and trap states. It is revealed that efficient and balanced transport is achieved in both $CH_3NH_3PbI_3$ neat film and $CH_3NH_3PbI_3/PC_{61}BM$ bilayer solar cells. Moreover, with the insertion of $PC_{61}BM$, both hole and electron mobilities of $CH_3NH_3PbI_3$ are doubled. This study offers a dynamic understanding of the operation of perovskite solar cells.

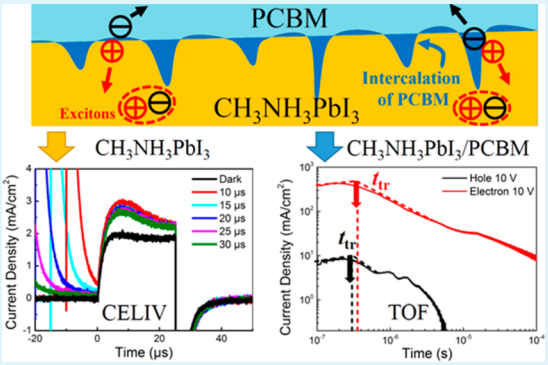

KEYWORDS: *perovskite, charge transport, CELIV, TOF, charge mobility, ambipolar*

There has very recently emerged a kind of "all-around" photovoltaic (PV) materials, hybrid organic−inorganic perovskites, which have rocked the solar cell field in the past two years alone.[1,2] Organometal halide perovskite ($APbX_3$, where A and X stand for a monovalent organic cation and halide anion, respectively), the most commonly studied of which are triiodide perovskite $CH_3NH_3PbI_3$, mixed halide perovskite $CH_3NH_3PbI_{3-x}Cl_x$ and $CH_3NH_3PbI_{3-x}Br_x$.[3] When used as light harvesting material, it offers practically all the desirable characteristics required in organic PVs such as large light absorption coefficient, tunable optical bandgap, low exciton binding energy, long exciton diffusion length, and long-range charge carrier lifetime.[4−6] Unique to perovskite materials are their unprecedented ambipolar charge mobilities; they are able to transport both holes and electrons effectively, thereby converting the absorbed photons into collected currents with close to 100% quantum efficiency.[7] With all these extraordinary properties, such hybrid organic−inorganic perovskite has now achieved a certified power conversion efficiency (PCE) of 20.1%,[8] making it very competitive with conventional thin-film PV technology.

Nonetheless, much of the fundamental photophysical mechanisms in driving the operation of high-performance perovskite PV device remains unanswered yet. Of critical importance are superior transport dynamics of perovskite materials. Recently, transient absorption,[6,9] photoluminescence-quenching,[5] impedance spectroscopy,[10] time-resolved microwave conductivity[11−13] and time-resolved terahertz spectroscopy[14] have been applied to study the photogeneration of excitons, and the transport and recombination of charge carriers. These studies showed that perovskite materials exhibited exciton diffusion lengths of >100 nm for $CH_3NH_3PbI_3$ and >1 μm for $CH_3NH_3PbI_{3-x}Cl_x$, high-frequency charge mobility of ~10 $cm^2\ V^{-1}\ s^{-1}$ as measured in contact-free film, extremely slow charge recombination on the time scale of microsecond, and a low trap density.[9−14] However, the dynamics of ambipolar charge transport characteristics in high-efficiency perovskite based solar cells still lacks of in-depth exploration.

Herein, we employed two complementary transport measurement methods—charge extraction by linearly increasing voltage (CELIV) and time-of-flight (TOF)—to uncover the ambipolar charge transport dynamics of the perovskite in the working solar cells.[15,16] Both CELIV and TOF have been used to measure quantitatively the charge transport dynamics of organic PV cells. CELIV can determine the mobility of faster charge carrier while elucidating the recombination process,[17] yet without the ability to distinguish the type of the charge carriers—hole or electron.[15] As a complementary method, TOF can determine the mobilities of both holes and electrons while revealing the trap states.[18] In this work, we studied the transport dynamics of $CH_3NH_3PbI_3$ perovskite as proof-of-concept in two representative planar devices—ITO/PEDOT:PSS/$CH_3NH_3PbI_3$/LiF/Al single-layer junction and ITO/PEDOT:PSS/$CH_3NH_3PbI_3$/phenyl-C61-butyric acid methyl ester ($PC_{61}BM$)/LiF/Al bilayer heterojunction. We

Received: January 5, 2015
Accepted: February 19, 2015
Published: February 19, 2015

DOI: 10.1021/acsami.5b00077
ACS Appl. Mater. Interfaces 2015, 7, 4471−4475

determine that efficient and balanced transport is achieved in both $CH_3NH_3PbI_3$ neat film and $CH_3NH_3PbI_3/PC_{61}BM$ bilayer systems, in the latter of which the transport of both holes and electrons are significantly improved after the insertion of $PC_{61}BM$. In addition, our results show that high-performance perovskite-based solar cells benefit from suppressed charge recombination, long lifetime of the mobile charge carriers, and absent shallow traps within $CH_3NH_3PbI_3$.

All perovskite films in the following discussion were prepared via one-step solution method in a similar way as reported previously[19] on PEDOT:PSS substrate, which resembles the device structure for reliable comparison. Optical absorption spectrum was first measured to confirm the formation of perovskite crystal structure. Figure 1a displays UV−vis absorption spectra of perovskite film, where two notable absorption bands are centered at ∼420 and 520 nm, accompanied by a shoulder peak at ca. 750 nm, typical of $CH_3NH_3PbI_3$.[20] X-ray diffraction (XRD) measurement was then conducted to further determine crystalline structures of perovskite film. As shown in Figure 1b, the as-synthesized sample exhibits characteristic peaks of 14.10 and 28.45°, corresponding to the (110) and (220) crystal planes of the $CH_3NH_3PbI_3$ structure, respectively.[19] These results suggest that the formation of perovskite crystals in as-prepared perovskite film is completed, which exhibits a high phase purity.

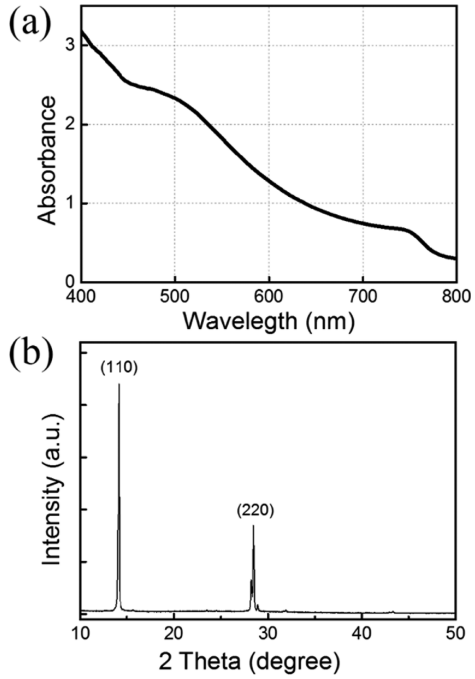

Figure 1. (a) UV−vis absorption spectrum and (b) X-ray diffraction pattern of $CH_3NH_3PbI_3$ perovskite film.

The planar perovskite solar cells were constructed with a typical device configuration of ITO/PEDOT:PSS/$CH_3NH_3PbI_3$ (250 nm)/$PC_{61}BM$ (30 nm)/LiF/Al with an active area of 0.11 cm^2 as shown in Figure 2a. Figure 2b displays the current density versus voltage ($J-V$) curves of $CH_3NH_3PbI_3$ planar PV cells. In the dark, the device shows a good diode behavior. Under AM 1.5G simulated light with an intensity of 100 mW cm^{-2}, a PCE of 9.2% was obtained with short-circuit current density (J_{SC}) of 16.10 mA cm^{-2}, open-circuit voltage (V_{OC}) of 0.84 V and fill factor (FF) of 68%.

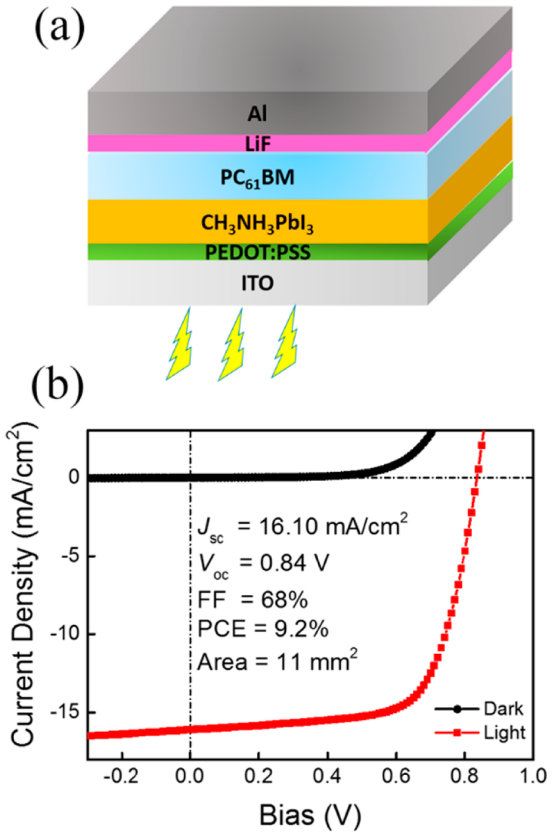

Figure 2. (a) Schematic of the perovskite solar cell configuration. (b) Representative current density−voltage characteristics of ITO/PEDOT:PSS/$CH_3NH_3PbI_3/PC_{61}BM$/LiF/Al planar cells in the dark and under AM 1.5G simulated light.

Moreover, this device exhibits negligible hysteresis under a scan rate of 10 mV/s and 50 mV/s, respectively, as shown in Figure S1 in the Supporting Information. Such performance is comparable to those literature reports based on similar or identical device structures.[21,22]

To understand the fundamental mechanisms underlying this high-performance perovskite solar cell, we studied the charge transport dynamics of this $CH_3NH_3PbI_3/PC_{61}BM$ bilayer heterojunction by CELIV and TOF, in comparison with $CH_3NH_3PbI_3$ single-layer junction, as shown in Figure 3. Note that the CELIV method is compatible with the film thickness of the active layer in the devices, whereas the TOF method requires relatively thick films of the active layer to ensure that the charge carriers traverse the depletion region to reach the accurate values of TOF mobility.[16]

Figure 3a, b shows the curves of CELIV current density vs time ($j-t$ profiles) of the $CH_3NH_3PbI_3$ neat film and $CH_3NH_3PbI_3/PC_{61}BM$ bilayer cell, respectively, with different delay times. Typically, the dark-CELIV measures the charge carriers induced by intrinsic impurities, while the photo-CELIV measures the photogenerated charge carriers.[15,16] The dark conductivity of the $CH_3NH_3PbI_3$ was measured as $\sim 1 \times 10^{-8}$ S/cm, which is 2 orders of magnitude lower than traditional conducting polymers (e.g., poly(3-hexyl-thiophene), P3HT).[23] Such low conductivity suggests that the $CH_3NH_3PbI_3$ perovskite has a notably low density of free charge carriers. In the dark $j-t$ profiles, as a result, the characteristic bump in CELIV is not evident, suggesting that there are almost no intrinsic impurities-induced charge carriers in both $CH_3NH_3PbI_3$ neat

DOI: 10.1021/acsami.5b00077
ACS Appl. Mater. Interfaces 2015, 7, 4471−4475

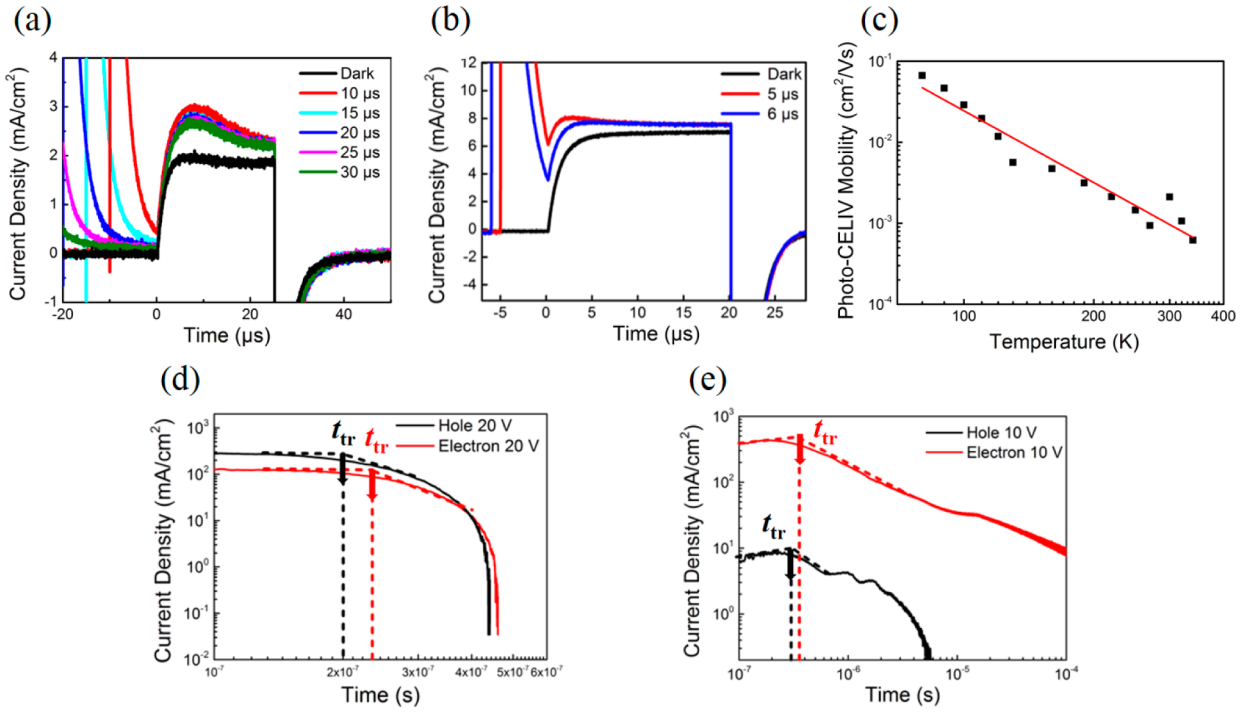

Figure 3. CELIV $j-t$ profiles with different delay times of (a) $CH_3NH_3PbI_3$ neat film at a voltage ramp of 2×10^4 V/s and (b) $CH_3NH_3PbI_3$/$PC_{61}BM$ bilayer cell at a voltage ramp of 1×10^5 V/s. (c) Temperature dependence of photo-CELIV mobility values of the $CH_3NH_3PbI_3$/$PC_{61}BM$ bilayer cell in a range of 80−340 K. TOF double logarithm $j-t$ profiles measuring the hole and electron mobilities of (d) $CH_3NH_3PbI_3$ neat film and (e) $CH_3NH_3PbI_3$/$PC_{61}BM$ bilayer cell at an applied bias of 20 and 10 V, respectively. Each t_{tr} is indicated by the arrow.

film and $CH_3NH_3PbI_3$/$PC_{61}BM$ bilayer cell. Upon light irradiation, the current density increases significantly and forms an obvious bump, indicating the creation of a large amount of photogenerated charge carriers, which allows for the mobility measurement as described below.

The mobility of the faster charge carrier measured by photo-CELIV was calculated from the following eq 1,[15] where μ is the charge mobility, d is the thickness of the active layer, $\Delta U/\Delta t$ is voltage ramp of the applied triangle voltage pulse, and t_{max} is the time when the value of the current density is maximum.

$$\mu = \frac{2d^2}{3\frac{\Delta U}{\Delta t}t_{max}^{\ 2}} \quad (1)$$

The results of photo-CELIV mobilities are summarized in Table S1 in the Supporting Information. The film thickness determined by scanning electron microscopy (SEM) imaging is ~250 nm. The ramp of the triangle voltage is 2×10^4 V/s and 1×10^5 V/s in the measurement of neat film and bilayer cell, respectively. The $CH_3NH_3PbI_3$ neat film exhibits the charge mobility of 3.2×10^{-4} $cm^2/(V\ s)$, and upon addition of the $PC_{61}BM$ layer, the charge mobility of bilayer cell is nearly doubled to 7.1×10^{-4} $cm^2/(V\ s)$. These mobility values which are determined from the OPV device structure largely differ from those of previously reported values[14] using other electrode-free methods. Moreover, as seen from the evolution of the $j-t$ profiles in $CH_3NH_3PbI_3$ neat film, maximum current density is slightly changed with varying the delay time in the range of 10−30 μs. This indicates a slow charge recombination in $CH_3NH_3PbI_3$ on the long time scale of 20 μs,[24] and a long lifetime of the mobile charge carriers in $CH_3NH_3PbI_3$, both of which contribute to the high-efficiency of perovskite cells.

To further explore the transport dynamics of perovskite solar cells, we studied the temperature dependence of photo-CELIV mobility in the $CH_3NH_3PbI_3$/$PC_{61}BM$ bilayer cell.[25] CELIV $j-t$ profiles of $CH_3NH_3PbI_3$/$PC_{61}BM$ bilayer film at temperatures ranging from 80 to 340 K are shown in Figure S2 in the Supporting Information. Note that 80 and 340 K correspond to the lowest temperature in liquid nitrogen and the possible onset degradation temperature of $CH_3NH_3PbI_3$, respectively. Data at each temperature was measured after specific temperature was reached and stabilized for >30 min. The profiles were obtained at a voltage ramp of 2.5×10^4 V/s with the same delay time of 6 μs. The temperature dependent photo-CELIV mobility values are summarized in Table S2 in the Supporting Information and plotted in Figure 3c in a double logarithm scale. At 340 K, $CH_3NH_3PbI_3$/$PC_{61}BM$ bilayer shows a CELIV mobility of 6.2×10^{-4} $cm^2/(V\ s)$, whereas up to 6.7×10^{-2} $cm^2/(V\ s)$ at 80 K. The data of log μ (mobility) vs log T (temperature) nicely fit a straight line as shown in Figure 3c, which follows an inverse power law temperature dependence of $\mu \propto T^{-n}$, where n is derived as 2.94. This is presumably indicative of bandlike conduction in $CH_3NH_3PbI_3$/$PC_{61}BM$ bilayer.[26]

However, the CELIV measurement cannot distinguish the type of charge carrier. By contrast, TOF method is able to measure both hole and electron mobility, independently. Figure 3d, e shows the double logarithm TOF $j-t$ profiles of $CH_3NH_3PbI_3$ neat film and $CH_3NH_3PbI_3$/$PC_{61}BM$ bilayer cell. The optimal voltage bias in the TOF measurements was found to be 20 and 10 V for the neat film and bilayer cell, respectively. To ensure the accuracy of the TOF mobility results, we increased the thickness of the $CH_3NH_3PbI_3$ layer in both neat film and bilayer cell to 400 nm from 250 nm in the CELIV measurement. The mobility of the charge carriers

DOI: 10.1021/acsami.5b00077
ACS Appl. Mater. Interfaces 2015, 7, 4471−4475

measured by TOF was calculated from the following eq 2,[16] where μ is the charge mobility, d is the thickness of the active layer, V is the voltage bias, and t_{tr} is the transient time.

$$\mu = \frac{d^2}{Vt_{tr}} \quad (2)$$

The results of TOF charge mobilities are summarized in Table S3 in the Supporting Information. Note that the small difference of the mobility results between CELIV and TOF is caused by the different film thickness of the perovskite layer.[27] In both $CH_3NH_3PbI_3$ neat film and $CH_3NH_3PbI_3/PC_{61}BM$ bilayer cell, the mobility values of holes and electrons are highly balanced. In the $CH_3NH_3PbI_3$ neat film, the hole and electron mobilities are 4.0×10^{-4} and 3.4×10^{-4} $cm^2/(V\ s)$, respectively, suggesting that $CH_3NH_3PbI_3$ is an ambipolar material and able to transport efficiently both holes and electrons. After introduction of the $PC_{61}BM$ layer in the bilayer cell, both hole and electron mobilities are increased to 5.4×10^{-4} and 4.5×10^{-4} $cm^2/(V\ s)$, respectively, and importantly remain highly balanced, which is consistent with our CELIV results. The enhanced charge mobility of perovskite with $PC_{61}BM$ is believed to closely relate to the interface between the perovskite and $PC_{61}BM$ layers.

SEM was used to support this assumption. Figure 4 displays the morphological differences between $CH_3NH_3PbI_3$ neat film and $CH_3NH_3PbI_3/PC_{61}BM$ bilayer film from top-view (Figure 4a, b) and cross-section (Figure 4c, d) SEM images. As shown in Figure 4a, the $CH_3NH_3PbI_3$ neat film consists of closely packed crystals with rough crystalline textures and full surface coverage. After spin-coating a thin layer of $PC_{61}BM$ on the top of $CH_3NH_3PbI_3$, the flat film is formed as seen in Figure 4b. On the other hand, cross-sectional SEM images also support that $PC_{61}BM$ not only fills the concaves of the surface of $CH_3NH_3PbI_3$ film but also forms a layer of $PC_{61}BM$ aggregate phase, thereby yielding an even and compact film with lower roughness compared to the neat film.[28] As schematically shown in Figure 4e, this intercalation phase of $PC_{61}BM$ can significantly increase the interface areas between $CH_3NH_3PbI_3$ and $PC_{61}BM$, thus facilitating the interfacial charge separation compared to the neat $CH_3NH_3PbI_3$ film.[28] Such $PC_{61}BM$ phase also contributes to the efficient extraction of the electrons, resulting in the high and balanced charge mobilities.

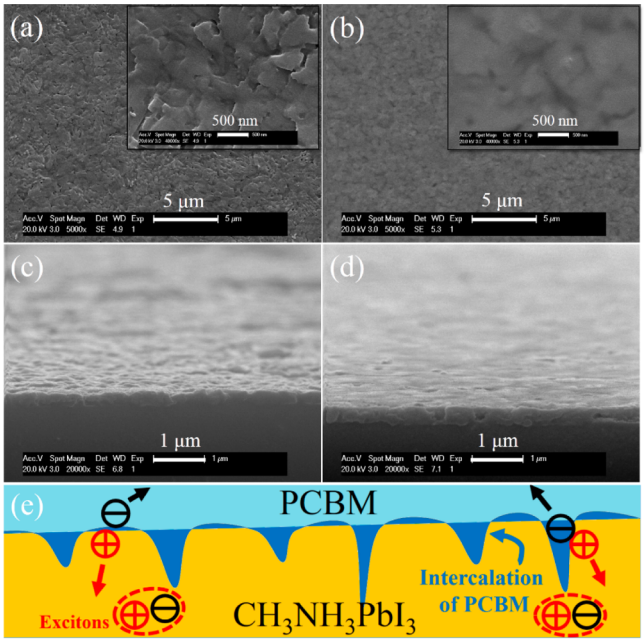

Figure 4. Top-view SEM images of (a) $CH_3NH_3PbI_3$ neat film and (b) $CH_3NH_3PbI_3/PC_{61}BM$ bilayer film, and tilted cross-sectional SEM images of (c) $CH_3NH_3PbI_3$ neat film and (d) $CH_3NH_3PbI_3/PC_{61}BM$ bilayer film. (e) Schematic depiction of the charge separation process in the bilayer structure of $CH_3NH_3PbI_3$ and $PC_{61}BM$.

The morphological differences also explain the trap states, which are revealed by the TOF results. Plateau region, which corresponds to the movement of photogenerated charge carriers through the bulk film, is intrinsically related to the trap states.[29] If there is more than one plateau regions in the TOF profiles, the first plateau results from the presence of deep traps, which does not influence the charge mobility, whereas the others are due to the existence of shallow traps, which would hinder charge transport.[29] As shown in Figure 3c, the $CH_3NH_3PbI_3$ neat film exhibits only one plateau region in both hole and electron $j-t$ profiles, indicating the absence of shallow traps in $CH_3NH_3PbI_3$. After introducing the $PC_{61}BM$ layer upon $CH_3NH_3PbI_3$, however, as shown in Figure 3d one additional plateau appears in the electron $j-t$ profile, suggesting the existence of shallow traps, whereas two extra plateaus appear in the hole $j-t$ profile, indicating the presence of more shallow traps. The shallow traps in the $CH_3NH_3PbI_3/PC_{61}BM$ bilayer are believed to originate from the defects caused by the addition of $PC_{61}BM$.[30] However, negative effects of shallow traps can be neglected compared to notably enhanced charge mobility with the addition of $PC_{61}BM$ because of improved charge separation and collection.

In conclusion, we have investigated the transport dynamics in both $CH_3NH_3PbI_3$ neat film and $CH_3NH_3PbI_3/PC_{61}BM$ bilayer systems using CELIV and TOF methods. High charge mobilities are found in both $CH_3NH_3PbI_3$ neat film and $CH_3NH_3PbI_3/PC_{61}BM$ bilayer cell. With the insertion of $PC_{61}BM$, both hole and electron mobilities of $CH_3NH_3PbI_3$ are doubled since the intercalation and aggregated phase of $PC_{61}BM$ can significantly enhance charge separation and thus increase the charge mobility. Our results indicate that efficient and balanced charge transport is achieved in high-performance $CH_3NH_3PbI_3$ solar cells, which results from suppressed recombination, long lifetime of the mobile charge carriers, and absent shallow traps within $CH_3NH_3PbI_3$.

■ ASSOCIATED CONTENT

Supporting Information

Detailed experimental procedures, Figures S1–S2, Tables S1–S3. This material is available free of charge via the Internet at http://pubs.acs.org.

■ AUTHOR INFORMATION

Corresponding Author

*E-mail: zqliang@fudan.edu.cn; 86-21-65642816.

Author Contributions

†Y.C. and J.P. contributed equally to this work.

Notes

The authors declare no competing financial interest.

■ ACKNOWLEDGMENTS

This work was supported by Recruitment Program of Global Experts in China, the start-up funds from Fudan University and

DOI: 10.1021/acsami.5b00077
ACS Appl. Mater. Interfaces 2015, 7, 4471–4475

National Natural Science Foundation of China (NSFC) Grant 51473036.

REFERENCES

(1) Kojima, A.; Teshima, K.; Shirai, Y.; Miyasaka, T. Organometal Halide Perovskites as Visible-Light Sensitizers for Photovoltaic Cells. *J. Am. Chem. Soc.* **2009**, *131*, 6050−6051.

(2) Snaith, H. J. Perovskites: The Emergence of a New Era for Low-Cost, High-Efficiency Solar Cells. *J. Phys. Chem. Lett.* **2013**, *4*, 3623−3630.

(3) Kojima, A.; Teshima, K.; Shirai, Y.; Miyasaka, T. Organometal Halide Perovskites as Visible-Light Sensitizers for Photovoltaic Cells. *J. Am. Chem. Soc.* **2009**, *131*, 6050−6051.

(4) Heo, J. H.; Im, S. H.; Noh, J. H.; Mandal, T. N.; Lim, C. S.; Chang, J. A.; Lee, Y. H.; Kim, H. J.; Sarkar, A.; Nazeeruddin, M. K.; Gratzel, M.; Seok, S. I. Efficient Inorganic−Organic Hybrid Heterojunction Solar Cells Containing Perovskite Compound and Polymeric Hole Conductors. *Nat. Photonics* **2013**, *7*, 486−491.

(5) Stranks, S. D.; Eperon, G. E.; Grancini, G.; Menelaou, C.; Alcocer, M. J. P.; Leijtens, T.; Herz, L. M.; Petrozza, A.; Snaith, H. J. Electron-Hole Diffusion Lengths Exceeding 1 Micrometer in an Organometal Trihalide Perovskite Absorber. *Science* **2013**, *342*, 341−344.

(6) Xing, G.; Mathews, N.; Sun, S.; Lim, S. S.; Lam, Y. M.; Grätzel, M.; Mhaisalkar, S.; Sum, T. C. Long-Range Balanced Electronand Hole-Transport Lengths in Organic-Inorganic $CH_3NH_3PbI_3$. *Science* **2013**, *342*, 344−347.

(7) Ball, J. M.; Lee, M. M.; Hey, A.; Snaith, H. J. Low-Temperature Processed Meso-Superstructured to Thin-Film Perovskite Solar Cells. *Energy Environ. Sci.* **2013**, *6*, 1739−1743.

(8) http://www.nrel.gov/ncpv/images/efficiency_chart.jpg.

(9) Kim, H.-S.; Lee, C.-R.; Im, J.-H.; Lee, K.-B.; Moehl, T.; Marchioro, A.; Moon, S.-J.; Humphry-Baker, R.; Yum, J.-H.; Moser, J. E.; Gratzel, M.; Park, N.-G. Lead Iodide Perovskite Sensitized All-Solid-State Submicron Thin Film Mesoscopic Solar Cell with Efficiency Exceeding 9%. *Sci. Rep.* **2012**, *2*, 591.

(10) Dualeh, A.; Moehl, T.; Tétreault, N.; Teuscher, J.; Gao, P.; Nazeeruddin, M. K.; Grätzel, M. Impedance Spectroscopic Analysis of Lead-Iodide Perovskite-Sensitized Solid-State Solar Cells. *ACS Nano* **2013**, *8*, 362−373.

(11) Oga, H.; Saeki, A.; Ogomi, Y.; Hayase, S.; Seki, S. Improved Understanding of the Electronic and Energetic Landscapes of Perovskite Solar Cells: High Local Charge Carrier Mobility, Reduced Recombination, and Extremely Shallow Traps. *J. Am. Chem. Soc.* **2014**, *136*, 13818−13825.

(12) Marchioro, A.; Teuscher, J.; Friedrich, D.; Kunst, M.; Krol, R. v. d.; Moehl, T.; Grätzel, M.; Moser, J.-E. Unravelling the Mechanism of Photoinduced Charge Transfer Processes in Lead Iodide Perovskite Solar Cells. *Nat. Photonics* **2014**, *8*, 250−255.

(13) Carlito S. Ponseca, J.; Savenije, T. J.; Abdellah, M.; Zheng, K.; Yartsev, A.; Pascher, T. r.; Harlang, T.; Chabera, P.; Pullerits, T.; Stepanov, A.; Wolf, J.-P.; Sundström, V. Organometal Halide Perovskite Solar Cell Materials Rationalized: Ultrafast Charge Generation, High and Microsecond-Long Balanced Mobilities, and Slow Recombination. *J. Am. Chem. Soc.* **2014**, *136*, 5189−5192.

(14) Wehrenfennig, C.; Eperon, G. E.; Johnston, M. B.; Snaith, H. J.; Herz, L. M. High Charge Carrier Mobilities and Lifetimes in Organolead Trihalide Perovskites. *Adv. Mater.* **2014**, *26*, 1584−1589.

(15) Pivrikas, A.; Sariciftci, N. S.; Juška, G.; Österbacka, R. A. Review of Charge Transport and Recombination in Polymer/Fullerene Organic Solar Cells. *Prog. Photovolt: Res. Appl.* **2007**, *15*, 677−696.

(16) Tiwari, S.; Greenham, N. C. Charge Mobility Measurement Techniques in Organic Semiconductors. *Opt. Quant. Electron* **2009**, *41*, 69−89.

(17) Juška, G.; Arlauskas, K.; Viliunas, M.; Genevicius, K.; Österbacka, R.; Stubb, H. Charge Transport in π-Conjugated Polymers from Extraction Current Transients. *Phys. Rev. B* **2000**, *62*, 16235−16238.

(18) Camaioni, N.; Tinti, F.; Esposti, A. D.; Righi, S.; Usluer, O.; Boudiba, S.; Egbe, D. A. M. Electron and Hole Transport in an Anthracene-Based Conjugated Polymers. *Appl. Phys. Lett.* **2012**, *101*, 053302.

(19) Zhao, Y.; Zhu, K. CH_3NH_3Cl-Assisted One-Step Solution Growth of $CH_3NH_3PbI_3$: Structure, Charge-Carrier Dynamics, and Photovoltaic Properties of Perovskite Solar Cells. *J. Phys. Chem. C* **2014**, *118*, 9412−9418.

(20) Seo, J.; Park, S.; Kim, Y. C.; Jeon, N. J.; Noh, J. H.; Yoon, S. C.; Seok, S. I. Benefits of very Thin PCBM and LiF Layer for Solution-Processed P-I-N Perovskite Solar Cells. *Energy Environ. Sci.* **2014**, *7*, 2642−2646.

(21) Jeng, J.-Y.; Chen, K.-C.; Chiang, T.-Y.; Lin, P.-Y.; Tsai, T.-D.; Chang, Y.-C.; Guo, T.-F.; Chen, P.; Wen, T.-C.; Hsu, Y.-J. Nickel Oxide Electrode Interlayer in $CH_3NH_3PbI_3$ Perovskite/PCBM Planar-Heterojunction Hybrid Solar Cells. *Adv. Mater.* **2014**, *26*, 4107−4113.

(22) Paek, S.; Cho, N.; Choi, H.; Jeong, H.; Lim, J. S.; Hwang, J.-Y.; Lee, J. K.; Ko, J. Improved External Quantum Efficiency from Solution-Processed $(CH_3NH_3)PbI_3$Perovskite/$PC_{71}BM$ Planar Heterojunction for High Efficiency Hybrid Solar Cells. *J. Phys. Chem. C* **2014**, *118*, 25899−25905.

(23) Liang, Z.; Reese, M. O.; Gregg, B. A. Chemically Treating Poly(3-hexylthiophene) Defects to Improve Bulk Heterojunction Photovoltaics. *ACS Appl. Mater. Interfaces* **2011**, *3*, 2042−2050.

(24) Chen, S.; Choudhury, K. R.; Subbiah, J.; Amb, C. M.; Reynolds, J. R.; So, F. Photo-Carrier Recombination in Polymer Solar Cells Based on P3HT and Silole-Based Copolymer. *Adv. Energy Mater.* **2011**, *1*, 963−969.

(25) Mozer, A. J.; Sariciftci, N. S.; Pivrikas, A.; Österbacka, R.; Juška, G.; Brassat, L.; Bässler, H. Charge Carrier Mobility in Regioregular Poly(3-hexylthiophene) Probed by Transient Conductivity Techniques: A comparative study. *Phys. Rev. B* **2005**, *71*, 035214.

(26) Coropceanu, V.; Cornil, J.; Filho, D. A. d. S.; Yoann Olivier, R. S.; Brédas, J.-L. Charge Transport in Organic Semiconductors. *Chem. Rev.* **2007**, *107*, 926−952.

(27) Yang, H.; Glynos, E.; Huang, B.; Green, P. F. Out-of-Plane Carrier Transport in Conjugated Polymer Thin Films: Role of Morphology. *J. Phys. Chem. C* **2013**, *117*, 9590−9597.

(28) Paek, S.; Cho, N.; Choi, H.; Jeong, H.; Lim, J. S.; Hwang, J.-Y.; Lee, J. K.; Ko, J. Improved External Quantum Efficiency from Solution-Processed $(CH_3NH_3)PbI_3$ Perovskite/$PC_{71}BM$ Planar Heterojunction for High Efficiency Hybrid Solar Cells. *J. Phys. Chem. C* **2014**, *118*, 25899−25905.

(29) Li, C.; Duan, L.; Li, H.; Qiu, Y. Universal Trap Effect in Carrier Transport of Disordered Organic Semiconductors: Transition from Shallow Trapping to Deep Trapping. *J. Phys. Chem. C* **2014**, *118*, 10651−10660.

(30) Awartani, O.; Kudenov, M. W.; Kline, R. J.; Brendan, T. O. In-Plane Alignment in Organic Solar Cells to Probe the Morphological Dependence of Charge Recombination. *Adv. Funct. Mater.* **2015**, DOI: 10.1002/adfm.201403377.

DOI: 10.1021/acsami.5b00077
ACS Appl. Mater. Interfaces 2015, 7, 4471−4475